Research Square

Preprints are preliminary reports that have not undergone peer review.
They should not be considered conclusive, used to inform clinical practice,
or referenced by the media as validated information.

Nuciferine induces ferroptosis and immunogenic cell death in hepatocellular carcinoma by targeting the TGF-βR1/SMAD3 axis

Hongwei Lan
Guizhou Provincial People's Hospital
Yang Zhou
Guangdong Provincial People's Hospital
Shuo Yao
Guangdong Provincial People's Hospital
Shifeng Pang
Guangdong Medical University
Jiayao Liu
704240349@qq.com

South China University of Technology

Research Article

Keywords: Nuciferine, Hepatocellular carcinoma, Ferroptosis, Metabolic reprogramming, Immunogenic cell death

Posted Date: November 23rd, 2026

DOI: https://doi.org/10.21203/rs.3.rs-11419025/v1

License: This work is licensed under a Creative Commons Attribution 4.0 International License.
Read Full License

Additional Declarations: No competing interests reported.

Nuciferine induces ferroptosis and immunogenic cell death in hepatocellular carcinoma by targeting the TGF-βR1/SMAD3 axis

Author names: Hongwei Lan[a], Yang Zhou[b], Shuo Yao[b], Shifeng Pang[d], Jiayao Liu[c]

Affiliations:

[a] *Department of Oncology, Guizhou Provincial People's Hospital, Guiyang, 550002, China.*

[b] *Guangdong Provincial People's Hospital, Guangzhou, 510006, China.*

[c]*South China University of Technology, Guangzhou, 510006, China.*

[d]*Department of Biotechnology, Guangdong Medical University, Guangzhou, 510006, China.*

Corresponding author. Shifeng Pang, Ph. D., Department of Biotechnology, Guangdong Medical University, No. 1 Xincheng Avenue, Songshan Lake Science and Technology Industry Park, Dongguan, Guangdong 523808, China.

E-mail address: psf1975@126.com.

Tel: +86-0769-22896398; Fax: +86-0769-22896227.

Corresponding author. Jiayao Liu, Ph. D., South China University of Technology, 381 Wushan Road, Tianhe District, Guangzhou 510641, China.

E-mail address: 704240349@qq.com.

Tel: +86-020-87111488; Fax: +86-020-87563007.

Abstract

Background: Nuciferine, an aporphine alkaloid from *Nelumbo nucifera*, exhibits broad anti-cancer activity, yet its direct protein target has remained elusive, precluding mechanism-based development. Whether TGF-βR1/SMAD3 signalling guards cancer cells against ferroptosis is likewise unknown.

Methods: Direct target engagement was examined by molecular docking, molecular dynamics simulations, CETSA, ITC and kinase activity assays. SMAD3-dependent transcription was interrogated by ChIP-qPCR and luciferase reporter assays. Ferroptosis, metabolic reprogramming, immunogenic cell death (ICD), dendritic cell phagocytosis and T-cell-mediated killing were evaluated in Hep3B and PLC/PRF/5 cells; antitumour efficacy was tested in subcutaneous and orthotopic Hepa1-6 models with an anti-PD-1 antibody or ferrostatin-1.

Results: Nuciferine directly bound TGF-βR1 (Kd = 2.3 ± 0.4 μmol/L; CETSA ΔTm = 2.7 °C) and inhibited its kinase activity (IC50 = 3.28 μmol/L), reducing SMAD3 phosphorylation. This uncovered a previously unrecognised mechanism whereby SMAD3 directly binds the GPX4 and SLC7A11 promoters to transcriptionally maintain ferroptosis defence; nuciferine dismantled this axis, collapsing antioxidant defence and triggering ferroptosis—reversed by ferrostatin-1—while suppressing glycolysis and mitochondrial respiration. The induced ferroptosis was immunogenic, promoting ATP/HMGB1 release, calreticulin exposure, dendritic cell phagocytosis and T-cell-mediated killing, partly through reduced lactate accumulation. Nuciferine selectively

killed HCC cells with minimal toxicity to THLE3 cells at 160 μmol/L, synergised with anti-PD-1 therapy, remodelled the tumour immune microenvironment and prolonged survival in orthotopic models, whereas ferrostatin-1 abrogated these benefits.

Conclusion: We identify TGF-βR1 as the direct protein target of nuciferine and reveal a SMAD3-GPX4/SLC7A11 transcriptional axis that guards HCC cells against ferroptosis. Pharmacological disruption of this node converts tumour cell death into an immunogenic, checkpoint-sensitising program, establishing nuciferine as a mechanistically defined lead for ferroptosis-based HCC therapy.

Keywords: Nuciferine; Hepatocellular carcinoma; Ferroptosis; Metabolic reprogramming; Immunogenic cell death.

Abbreviation	Full name
CETSA	cellular thermal shift assay
CFSE	carboxyfluorescein succinimidyl ester
ChIP	chromatin immunoprecipitation
CRT	calreticulin
DC	dendritic cell
ECAR	extracellular acidification rate
ICD	immunogenic cell death
ITC	isothermal titration calorimetry
MD	molecular dynamics
OCR	oxygen consumption rate
PBMC	peripheral blood mononuclear cell
PD-1	programmed cell death protein 1
PKM2	pyruvate kinase M2
RMSD	root-mean-square deviation
ROS	reactive oxygen species

Introduction

Hepatocellular carcinoma (HCC) represents the predominant form of primary liver cancer and ranks among the leading causes of cancer-related death globally (Bray et al., 2024). Despite advances in surgical resection, liver transplantation, and targeted therapies (Cheng et al., 2022; Ganesan and Kulik, 2023; Llovet et al., 2022), the prognosis for advanced HCC remains dismal due to high rates of recurrence and metastasis (Aldea et al., 2021; Sun et al., 2021). Therefore, the exploration of novel therapeutic strategies with distinct mechanisms of action is urgently warranted.

Ferroptosis is a recently identified form of regulated cell death driven by iron-dependent lipid peroxidation and characterized by the accumulation of reactive oxygen species (ROS) and lipid peroxides (Tang et al., 2021; Wang et al., 2021; Wang et al., 2023). Unlike apoptosis or autophagy, ferroptosis is morphologically and biochemically distinct, rendering it an attractive target for circumventing conventional drug resistance in cancer therapy (Tang et al., 2021; Viswanathan et al., 2017). The core regulatory network of ferroptosis centers on glutathione peroxidase 4 (GPX4) and system Xc^- (comprising SLC7A11 and SLC3A2), which cooperatively suppress lipid peroxidation (Dai et al., 2024). Inhibition of this axis leads to overwhelming oxidative stress and subsequent cell death (Viswanathan et al., 2017). Accumulating evidence suggests that inducing ferroptosis in HCC cells represents a viable therapeutic strategy, particularly for tumors resistant to conventional chemotherapy (Huang et al., 2023; Zhou et al., 2024).

Nuciferine is a major aporphine alkaloid isolated from the leaves of *Nelumbo nucifera Gaertn*, a traditional medicinal herb widely used in East Asia (Zhao et al., 2023). Previous studies have reported that nuciferine possesses anti-inflammatory, anti-obesity, and anti-cancer properties (Guo et al., 2013; Xie et al., 2023; Zhao et al., 2023). However, its precise molecular mechanism in HCC, particularly its potential role in regulating cell death modalities such as ferroptosis, remains poorly understood (Zhao et al., 2023). The transforming growth factor-beta (TGF-β) signaling pathway, mediated by TGF-β receptor 1 (TGF-βR1) and downstream SMAD transcription factors, plays a pivotal role in tumor progression, immune evasion, and metabolic adaptation (Massagué, 2012; Peng et al., 2022). Interestingly, emerging studies have linked TGF-β/SMAD signaling to the modulation of ferroptosis sensitivity in cancer cells (Peng et al., 2022). In this study, we demonstrate that nuciferine exerts potent anti-HCC activity by inducing ferroptosis and metabolic reprogramming. Through an integrative approach combining computational docking, biophysical assays, and molecular biology, we identified TGF-βR1 as a direct protein target of nuciferine. Nuciferine binding to TGF-βR1 inhibits SMAD3 activation, thereby relieving SMAD3-mediated transcriptional activation of GPX4 and SLC7A11, dismantling the cellular antioxidant defense system and triggering ferroptosis. Our findings establish a previously unrecognized mechanism linking the TGF-βR1/SMAD3 axis to ferroptosis regulation and position nuciferine as a promising lead compound for ferroptosis-based HCC therapy.

Method

Cell culture and reagents

Hep3B, PLC/PRF/5, and THLE3 cells were maintained in DMEM or RPMI-1640 supplemented with 10% FBS. Nuciferine (purity > 98%) was dissolved in DMSO. Ferrostatin-1 and Z-VAD-FMK were purchased from APEBIO. The purity of nuciferine (> 98%) was verified by high-performance liquid chromatography (HPLC), as shown in **Supplementary Fig. S1.**

Cell viability and proliferation

CCK-8 assays and EdU incorporation assays were performed according to standard protocols.

Seahorse analysis

Oxygen consumption rate (OCR) and extracellular acidification rate (ECAR) were measured using the Seahorse XF96 Extracellular Flux Analyzer. Cells were seeded into XF96 plates at 1×10^4 cells/well and treated with nuciferine for 24 h; OCR and ECAR were recorded after sequential injection of oligomycin, FCCP, and rotenone/antimycin A. Intracellular pyruvate and lactate levels in cell lysates were determined colorimetrically using commercial assay kits according to the manufacturers' protocols.

Ferroptosis assessment

Intracellular ROS was detected by DCFH-DA staining. MDA levels were quantified using a lipid peroxidation assay kit. Protein expression was analyzed by western

blotting using antibodies against ACSL4, GPX4, SLC7A11, p-SMAD2/3, and GAPDH.

Immunogenic cell death assessment

Extracellular ATP released into the culture supernatant was measured using a luciferase-based ATP assay kit, and HMGB1 release was quantified by ELISA according to the manufacturers' protocols. Calreticulin (CRT) exposure on the cell surface was detected by immunofluorescence staining. Staurosporine (STS) and mitoxantrone were used as reference treatments where indicated.

DC phagocytosis assay

Hep3B cells were labeled with CFSE and treated with nuciferine with or without ferrostatin-1, then co-cultured with CD11c+ dendritic cells. Phagocytosis was quantified by flow cytometry as the percentage of CD11c+CFSE+ cells.

Tumor cell–PBMC co-culture and T-cell cytotoxicity assay

Peripheral blood mononuclear cells (PBMCs) were co-cultured with nuciferine-treated Hep3B or PLC/PRF/5 cells as illustrated in Figure 6A. T-cell cytotoxicity against tumor cells was quantified, and the proportions of GZMB+, IFN-γ+, and TNF-α+ cells among CD8+ T cells were analyzed by flow cytometry. Where indicated, lactic acid was added to the co-culture system.

Flow cytometric analysis of tumor-infiltrating immune cells

Tumors were excised, minced, and digested into single-cell suspensions. Cells were stained with fluorochrome-conjugated antibodies against CD4, CD8, GZMB, IFN-γ, TNF-α, Tim-3, LAG-3, PD-1, CD11c, CD103, CD40, and MHC II, and analyzed by flow cytometry.

Molecular docking

The three-dimensional structure of TGF-βR1 (PDB ID: 3HMM) was retrieved from the RCSB Protein Data Bank and prepared in AutoDockTools by removing water molecules and adding hydrogen atoms. The nuciferine structure (PubChem CID: 161068) was optimized using Chem3D. Docking was performed with AutoDock Vina 1.1.2 using a 60 × 60 × 60 Å grid box centered on the ATP-binding pocket, and the lowest-energy conformation was selected for visualization.

Molecular dynamics simulations

MD simulations were conducted using GROMACS 2020.6 with the AMBER99SB-ILDN force field. The nuciferine–TGF-βR1 complex was solvated in a TIP3P water box (minimum 1.0 nm from the box edge) and neutralized with Na^+/Cl^- ions. After steepest-descent energy minimization and equilibration (100 ps NVT, then 100 ps NPT), a 100-ns production run was performed at 300 K and 1 bar. RMSD and Rg were calculated using GROMACS built-in tools.

CETSA

Cellular thermal shift assay was performed as described previously with minor modifications. Hep3B cell lysates were incubated with nuciferine (40 μmol/L) or DMSO for 30 min at room temperature. The samples were then aliquoted and heated at indicated temperatures (37–62 °C) for 3 min, followed by cooling at room temperature for 3 min. After centrifugation at 12,000 × g for 20 min, the supernatants were analyzed by Western blotting using an anti-TGF-βR1 antibody.

ITC

Isothermal titration calorimetry was performed on a MicroCal PEAQ-ITC instrument (Malvern Panalytical) at 25 °C. Nuciferine (200 μmol/L) was titrated into recombinant TGF-βR1 protein (20 μmol/L) in 20 successive injections of 2 μL each, with a spacing of 150 s between injections. The data were analyzed using the MicroCal PEAQ-ITC Analysis Software, and the binding parameters were fitted to a one-site binding model.

ChIP-qPCR

ChIP was performed as described previously with minor modifications. Hep3B cells at approximately 80% confluence were cross-linked with 1% formaldehyde for 10 min at room temperature and quenched with 125 mM glycine. Cell pellets were lysed in buffer (1% SDS, 10 mM EDTA, 50 mM Tris-HCl, pH 8.1, with protease inhibitor cocktail), and chromatin was sheared to 200–500 bp by sonication (Bioruptor; 30 cycles of 10 s on/20 s off at 30% amplitude). Sheared chromatin (500 μg) was immunoprecipitated

overnight at 4 °C with 5 μg of anti-SMAD3 antibody (Abcam, ab208182) or normal rabbit IgG (Cell Signaling Technology, #2729) pre-bound to 50 μL of Protein A/G magnetic beads. The beads were washed sequentially with low-salt, high-salt, LiCl, and TE buffers; complexes were eluted with elution buffer (1% SDS, 0.1 M $NaHCO_3$) at 65 °C, and cross-links were reversed with 200 mM NaCl at 65 °C overnight. After proteinase K treatment (45 °C, 1 h), DNA was purified by phenol-chloroform extraction and ethanol precipitation and resuspended in nuclease-free water.

Quantitative PCR was performed using SYBR Green Master Mix (Thermo Fisher Scientific) on a QuantStudio 6 Flex Real-Time PCR System (Applied Biosystems) with primers targeting the putative SMAD3-binding elements (SBEs) in the GPX4 and SLC7A11 promoters: GPX4 site 2 forward, 5'-AGCTGTCACCTGATCCCTGAA-3', and reverse, 5'-TGGAAGGGAGAGAGAGGAGA-3'; GPX4 site 3 forward, 5'-CCTTCCTGCTCCTGCTTCTT-3', and reverse, 5'-GAGGGAGGGAGGGAGAGAGT-3'; SLC7A11 site 1 forward, 5'-GCCTGGTCTGAACTCCTGAC-3', and reverse, 5'-CAGGAGGCGAGAGAGAGAGA-3'. Relative enrichment was calculated by the 2^(-ΔCt) method normalized to the IgG control. All experiments were performed in triplicate and repeated independently at least three times.

Animal studies

Animal studies were approved by the Ethics Committee of Guangdong Provincial People's Hospital (S2024-816-01). Male C57BL/6J mice (6 weeks old, 18–22 g;

GemPharmatech, Nanjing, China) were housed under SPF conditions with free access to standard chow and water. For the subcutaneous model, Hepa1-6 cells were injected into the right flank, and tumor-bearing mice were randomized into four groups: control, nuciferine (100 mg/kg, intraperitoneally, every 3 days), anti-PD-1 monoclonal antibody (mAb), and nuciferine plus anti-PD-1 mAb. Tumor volume ($V = \text{length} \times \text{width}^2 / 2$) was measured every 3 days using a digital caliper. Mice were sacrificed on day 21, and tumors were excised, weighed, and subjected to immunohistochemistry, immunofluorescence, western blotting, and flow cytometric analysis of tumor-infiltrating immune cells. For the orthotopic model, Hepa1-6-Luc cells were implanted into the liver, and mice were treated with nuciferine (100 mg/kg, every 3 days) with or without ferrostatin-1. Tumor burden was monitored by IVIS bioluminescence imaging on days 0, 7, 14, and 21, and overall survival was recorded.

Statistical analysis

Data are presented as mean ± SD from at least three independent biological replicates unless otherwise indicated. Statistical significance was determined by Student's t-test for comparisons between two groups and by one-way ANOVA followed by Tukey's post hoc test for multiple comparisons. Tumor growth curves were analyzed by two-way ANOVA, and survival curves were compared using the log-rank (Mantel–Cox) test. All analyses were performed using GraphPad Prism 11.0. $P < 0.05$ was considered statistically significant.

Results

Nuciferine inhibits HCC cell proliferation

To evaluate the anti-proliferative effect of nuciferine on HCC, we first examined its cytotoxicity in normal human hepatocyte THLE3 and HCC cell lines (Hep3B and PLC/PRF/5). As shown in **Figure 1B,** nuciferine exhibited minimal cytotoxicity toward THLE3 cells even at 160 μmol/L, whereas it significantly reduced the viability of Hep3B and PLC/PRF/5 cells in a concentration-dependent manner. Time-course proliferation assays further confirmed that nuciferine treatment (10–40 μmol/L) markedly suppressed the proliferation of both Hep3B **(Figure 1C)** and PLC/PRF/5 **(Figure 1D)** cells over 3–4 days. EdU incorporation assay revealed a dose-dependent decrease in the proportion of proliferating cells in both cell lines **(Figure 1E–H),** indicating that nuciferine effectively inhibits HCC cell proliferation.

Nuciferine induces metabolic reprogramming in HCC cells

To explore the mechanisms underlying nuciferine-induced growth inhibition, we performed transcriptomic profiling of nuciferine-treated HCC cells. Principal component analysis (PCA) revealed a clear separation between control and nuciferine-treated samples **(Figure 2A),** and KEGG enrichment analysis of differentially expressed genes revealed significant alterations in metabolic pathways, including glycolysis and the Warburg effect **(Figure 2B).** Nuciferine treatment significantly reduced intracellular lactic acid content **(Figure 2E)** while increasing pyruvic acid accumulation **(Figure 2F)** in both Hep3B and PLC/PRF/5 cells. Seahorse metabolic flux analysis further demonstrated that nuciferine markedly decreased both the oxygen consumption rate (OCR) and the extracellular acidification rate (ECAR) in both cell

lines **(Figure 2G, H)**, indicating impaired mitochondrial respiration and glycolytic capacity. Consistently, Western blot analysis showed downregulation of key glycolytic enzymes, including hexokinase 2 (HK2), pyruvate kinase M2 (PKM2), and lactate dehydrogenase A (LDHA), in nuciferine-treated cells **(Figure 2I, J)**. Notably, nuciferine also dose-dependently downregulated the ferroptosis suppressors SLC7A11 and GPX4 while upregulating ACSL4 **(Figure 2C, D)**, suggesting concomitant activation of ferroptosis. These results collectively suggest that nuciferine suppresses HCC cell proliferation, at least in part, by inducing metabolic reprogramming and inhibiting glycolysis.

Nuciferine induces ferroptosis in HCC cells

To determine whether nuciferine-induced cell death occurs via ferroptosis, we examined canonical ferroptotic hallmarks. Nuciferine treatment significantly elevated intracellular ROS levels **(Figure 3A)** and increased the lipid peroxidation product MDA in a dose-dependent manner in both Hep3B and PLC/PRF/5 cells **(Figure 3B, C)**. Notably, the ferroptosis-specific inhibitor ferrostatin-1, but not the apoptosis inhibitor Z-VAD-FMK or the necroptosis inhibitor necrostatin-1, effectively rescued nuciferine-induced cell death **(Figure 3F, G).** Consistently, ferrostatin-1 restored the protein levels of SLC7A11 and GPX4 suppressed by nuciferine **(Figure 3D, E).** Furthermore, transmission electron microscopy demonstrated that nuciferine-treated cells exhibited typical ferroptotic mitochondrial morphology, including mitochondrial shrinkage, increased membrane density, and loss of cristae **(Figure 3H)**. Collectively, these

findings indicate that nuciferine induces ferroptosis in HCC cells.

Nuciferine directly binds to TGF-β R1 and inhibits its kinase activity and downstream SMAD3 signaling

To elucidate the direct molecular target of nuciferine, we performed molecular docking and molecular dynamics (MD) simulations. Nuciferine was predicted to stably occupy the ATP-binding pocket of TGF-βR1 through hydrophobic interactions and hydrogen bonding with key residues **(Figure 4A)**. MD simulation analysis revealed that the TGF-βR1–nuciferine complex maintained low Rg and RMSD values throughout the 100-ns trajectory, indicating a stable binding conformation, whereas complexes with TGF-βR2, GPX4, or SLC7A11 exhibited higher fluctuations **(Figure 4B, C)**. The cellular thermal shift assay (CETSA) further confirmed that nuciferine significantly increased the thermal stability of TGF-βR1, with a ΔTm of 2.7 °C **(Figure 4D, E)**. Isothermal titration calorimetry (ITC) demonstrated a direct and high-affinity interaction between nuciferine and TGF-βR1, with a Kd of 2.3 ± 0.4 μmol/L **(Figure 4F)**. Functionally, nuciferine potently inhibited TGF-βR1 kinase activity in a dose-dependent manner, yielding an IC50 of 3.28 μmol/L **(Figure 4G).**

Consistent with target engagement, nuciferine dose-dependently decreased the expression of TGF-βR1 and reduced the phosphorylation of SMAD2/3 in both Hep3B and PLC/PRF/5 cells, without affecting TGF-βR2 or total SMAD2/3 levels **(Figure 4H, I)**. Notably, pharmacological inhibition of TGF-βR1 (RepSox) or SMAD3 (SIS3) partially attenuated nuciferine-induced cytotoxicity, and the combination of nuciferine with either inhibitor produced no additive effect **(Figure 4J, K)**, consistent with

nuciferine acting through the TGF-βR1/SMAD3 axis. Moreover, RepSox reversed the nuciferine-mediated downregulation of SLC7A11 and GPX4 **(Figure 4L, M)**. Taken together, these data identify TGF-βR1 as a direct target of nuciferine and indicate that nuciferine exerts its anti-tumor and pro-ferroptotic effects, at least partially, through suppression of the TGF-βR1/SMAD3 signaling pathway.

SMAD3 transcriptionally regulates GPX4 and SLC7A11 in HCC cells

To explore the molecular mechanism linking TGF-βR1/SMAD3 signaling to nuciferine-induced ferroptosis, we investigated whether SMAD3 transcriptionally regulates ferroptosis-related genes. Bioinformatics analysis identified several putative SMAD3-binding elements (SBEs) within the promoter regions of both GPX4 and SLC7A11 **(Supplementary Fig. S2A)**. Chromatin immunoprecipitation (ChIP)-qPCR assays confirmed that SMAD3 directly bound to the GPX4 and SLC7A11 promoters, particularly at binding sites 2 and 3 **(Supplementary Fig. S2B)**. Dual-luciferase reporter assays demonstrated that SMAD3 overexpression significantly enhanced the transcriptional activity of both promoters, whereas SMAD3 knockdown abolished this effect. Importantly, nuciferine treatment markedly suppressed the promoter activities, and this suppression was partially rescued by SMAD3 overexpression **(Supplementary Fig. S2C).** Furthermore, silencing of SMAD3 significantly attenuated the basal expression of GPX4 and SLC7A11 and abrogated the nuciferine-induced downregulation of these genes at the mRNA level **(Supplementary Fig. S2D)**. These findings establish that SMAD3 directly binds to the promoters of GPX4 and SLC7A11 to activate their transcription, and that nuciferine disrupts this transcriptional axis by

inhibiting TGF-βR1/SMAD3 signaling, thereby promoting ferroptosis.

Nuciferine-induced ferroptosis elicits immunogenic cell death and promotes dendritic cell phagocytosis

Ferroptosis has recently been recognized as a form of immunogenic cell death (ICD). We therefore examined whether nuciferine-induced ferroptosis elicits ICD in HCC cells. Nuciferine treatment dose-dependently increased the extracellular release of ATP **(Figure 5A)** and HMGB1 **(Figure 5B)** and promoted calreticulin (CRT) exposure on the cell surface **(Figure 5C)** in both Hep3B and PLC/PRF/5 cells—the three hallmark damage-associated molecular patterns (DAMPs) of ICD. These effects were largely abrogated by the ferroptosis inhibitors ferrostatin-1 and deferoxamine (DFO) **(Figure 5D, E),** indicating that ICD induction is a downstream consequence of ferroptosis. Reference ICD inducers, including staurosporine (STS) and mitoxantrone, produced comparable levels of growth inhibition under these conditions **(Figure 5G)**. Functionally, dendritic cells efficiently phagocytosed CFSE-labeled, nuciferine-treated Hep3B cells, whereas ferrostatin-1 markedly reduced this phagocytosis **(Figure 5H, I)**. These data demonstrate that nuciferine-induced ferroptosis is immunogenic and promotes DC-mediated engulfment of dying tumor cells.

Nuciferine enhances T-cell-mediated killing of HCC cells, an effect attenuated by lactic acid

We next asked whether nuciferine-treated tumor cells are more susceptible to T-cell-mediated killing. In a tumor cell–PBMC co-culture system **(Figure 6A),** nuciferine treatment dose-dependently increased the cytotoxicity of T cells against both Hep3B

and PLC/PRF/5 cells **(Figure 6B)**. Mechanistically, nuciferine-treated tumor cells enhanced the effector function of co-cultured CD8+ T cells, reflected by increased proportions of granzyme B (GZMB)-, IFN-γ-, and TNF-α-positive CD8+ T cells **(Figure 6C–F)**. Given that nuciferine suppresses glycolysis-derived lactate production **(Figure 2E)** and that extracellular lactate blunts T-cell-mediated immunosurveillance, we tested whether lactate mediates this effect. Supplementation with lactic acid partially reversed the nuciferine-induced enhancement of T-cell effector function **(Figure 6C–F),** indicating that nuciferine potentiates T-cell-mediated tumor killing at least in part by alleviating lactate-mediated immunosuppression.

Nuciferine synergizes with anti-PD-1 therapy to suppress HCC growth in immunocompetent mice

To evaluate the anti-tumor efficacy of nuciferine in an immunocompetent setting and its potential synergy with immune checkpoint blockade, we established a subcutaneous Hepa1-6 tumor model in C57BL/6J mice. Tumor-bearing mice were treated with nuciferine (100 mg/kg, every 3 days), an anti-PD-1 monoclonal antibody (mAb), or their combination for 21 days **(Figure 7A)**. Both nuciferine and anti-PD-1 mAb monotherapies significantly suppressed tumor growth, while the combination achieved the strongest tumor inhibition, as evidenced by tumor size, growth curves, and tumor weight **(Figure 7B–D).** Immunofluorescence staining revealed that the combination treatment markedly increased intratumoral infiltration of CD8+ T cells and their expression of TNF-α and IFN-γ **(Figure 7E).** Immunohistochemical staining showed that nuciferine and anti-PD-1 mAb, alone or in combination, markedly reduced

the proliferation marker Ki67 and the ferroptosis suppressor GPX4 in tumor tissues **(Figure 7F).** Consistently, Western blot analysis of tumor lysates demonstrated that the combination treatment upregulated ACSL4 and the ICD markers CRT and HMGB1, while downregulating GPX4, the glycolytic enzyme HK2, and Ki67 **(Figure 7G)**. Collectively, these in vivo data demonstrate that nuciferine synergizes with anti-PD-1 therapy to suppress HCC growth, accompanied by enhanced ferroptosis, suppressed glycolysis, and activation of anti-tumor immunity.

Nuciferine combined with anti-PD-1 therapy remodels the tumor immune microenvironment

To characterize the tumor immune microenvironment, we performed flow cytometric analysis of tumor-infiltrating immune cells. Nuciferine treatment increased the proportion of intratumoral CD8+ T cells, and the combination with anti-PD-1 mAb further augmented CD8+ T-cell infiltration **(Figure 8A)**. The frequencies of GZMB+ and IFN-γ+ CD8+ T cells were significantly elevated in the nuciferine and combination groups **(Figure 8B)**, whereas the proportions of exhausted CD8+ T cells expressing Tim-3, LAG-3, and PD-1 were markedly reduced **(Figure 8C).** In addition, nuciferine promoted the infiltration and activation of dendritic cells, as indicated by increased proportions of CD11c+ DCs (Figure 8D), CD11c+CD103+ DCs **(Figure 8E)**, and DCs expressing the maturation markers CD40 and MHC II **(Figure 8F)**, with the combination group showing the most pronounced effects. These results indicate that nuciferine remodels the tumor immune microenvironment toward an inflamed, T-cell- and DC-activated state, thereby sensitizing HCC to PD-1 blockade.

Nuciferine suppresses orthotopic HCC growth and activates anti-tumor immunity in a ferroptosis-dependent manner

Finally, we established an orthotopic Hepa1-6-Luc liver tumor model in C57BL/6J mice to validate the ferroptosis dependence of the anti-tumor activity of nuciferine in vivo **(Figure 9A)**. Mice were treated with nuciferine with or without the ferroptosis inhibitor ferrostatin-1, and tumor burden was monitored longitudinally by IVIS bioluminescence imaging **(Figure 9B)**. Nuciferine markedly suppressed intrahepatic tumor growth, as reflected by reduced luciferase activity, whereas ferrostatin-1 co-treatment largely reversed this effect **(Figure 9C)**. Accordingly, nuciferine significantly prolonged overall survival, and this survival benefit was abrogated by ferrostatin-1 ($P = 0.0304$; **Figure 9I**). Flow cytometric analysis of orthotopic tumors revealed that nuciferine increased the infiltration and effector function of CD8+ T cells (GZMB, IFN-γ, TNF-α; **Figure 9D**) and promoted DC infiltration and maturation (CD11c+ and CD11c+MHCII+; **Figure 9E, F**), effects that were largely reversed by ferrostatin-1. These findings establish that nuciferine suppresses orthotopic HCC growth and activates anti-tumor immunity in a ferroptosis-dependent manner.

Discussion

Ferroptosis has garnered substantial attention as a vulnerability in solid tumors, including HCC, which often exhibits inherent resistance to apoptosis (Overchuk et al., 2025; Tang et al., 2021; Zhou et al., 2024). In this study, we reveal that nuciferine, a natural aporphine alkaloid, functions as a potent ferroptosis inducer in HCC through a

mechanism involving direct targeting of TGF-βR1 and subsequent inhibition of SMAD3-mediated transcriptional activation of GPX4 and SLC7A11. This work not only elucidates the anti-HCC mechanism of nuciferine but also establishes a novel functional link between TGF-βR1/SMAD3 signaling and ferroptosis regulation (Massagué, 2012; Peng et al., 2022).

By integrating computational docking, MD simulations, CETSA, and ITC, we identified TGF-βR1 as a direct protein target of nuciferine, addressing a longstanding challenge in natural product pharmacology (Zhao et al., 2023). Nuciferine binding inhibits TGF-βR1 kinase activity and reduces SMAD2/3 phosphorylation, consistent with the tumor-promoting role of TGF-βR1 in HCC (Massagué, 2012; Peng et al., 2022). Whereas SMAD3 activation normally maintains the expression of ferroptosis defense genes, nuciferine disrupts this protective axis and shifts the cellular balance toward ferroptotic death.

Metabolic reprogramming is a hallmark of cancer and a prerequisite for rapid proliferation (Brand et al., 2016; Hanahan, 2022). Our Seahorse metabolic flux analysis revealed that nuciferine globally suppresses both oxidative phosphorylation and glycolysis in HCC cells. The accumulation of pyruvate alongside decreased lactate suggests a potential blockade in lactate dehydrogenase (LDH) activity or a diversion of glycolytic intermediates (Brand et al., 2016; Chen et al., 2024). This metabolic paralysis likely contributes to ferroptosis sensitivity, as cancer cells with impaired metabolic plasticity are less capable of generating the reducing equivalents (NADPH and GSH) necessary to sustain GPX4 activity (Dai et al., 2024; Galluzzi et al., 2017; Tang et al.,

412 2021).

413 The transcriptional mechanism uncovered herein—inhibition of SMAD3-
414 mediated transcriptional activation of GPX4 and SLC7A11—provides a plausible
415 explanation for how TGF-β signaling can modulate ferroptosis. While TGF-β is
416 classically known to regulate epithelial-mesenchymal transition (EMT) and immune
417 suppression (Massagué, 2012; Peng et al., 2022), its role in ferroptosis has only recently
418 begun to emerge (Huang et al., 2023; Zhou et al., 2025). Our ChIP-qPCR data
419 demonstrate that SMAD3 occupies specific regions within the promoters of GPX4 and
420 SLC7A11, leading to their transcriptional upregulation. This reveals a cytoprotective
421 function of SMAD3 in maintaining ferroptosis resistance, which nuciferine disrupts.

422 Beyond its direct cytotoxic effects, nuciferine-induced ferroptosis is immunogenic.
423 Ferroptotic HCC cells released ATP and HMGB1 and exposed surface CRT—canonical
424 damage-associated molecular patterns that promote dendritic cell recruitment,
425 phagocytosis, and antigen presentation (Galluzzi et al., 2017; Zitvogel et al., 2011).
426 Consistently, nuciferine-treated tumor cells were efficiently phagocytosed by DCs and
427 became more susceptible to T-cell-mediated killing, an effect partly attributable to
428 reduced lactate accumulation (Brand et al., 2016). These in vitro observations translated
429 into therapeutic benefit in vivo: in immunocompetent Hepa1-6 models, nuciferine
430 increased intratumoral CD8+ T-cell infiltration and effector function, reduced T-cell
431 exhaustion, promoted DC infiltration and maturation, and synergized with anti-PD-1
432 therapy. Importantly, ferrostatin-1 reversed both the anti-tumor efficacy and the
433 immune activation elicited by nuciferine in the orthotopic model, establishing

ferroptosis as the upstream event coupling nuciferine treatment to anti-tumor immunity (Bruni et al., 2020; Chryplewicz et al., 2022; Galon et al., 2013; Qiu et al., 2024; Xiong et al., 2023; Zhou et al., 2025).

From a translational perspective, nuciferine represents an attractive candidate for further development. Its natural origin, favorable safety profile, and dual capacity to induce ferroptosis and activate anti-tumor immunity position it as a multifunctional agent for HCC therapy (Guo et al., 2013; Zhao et al., 2023). Future studies should focus on optimizing its pharmacokinetic properties and evaluating its efficacy in combination with immune checkpoint inhibitors or other ferroptosis inducers (Llovet et al., 2022; Xiong et al., 2023).

In conclusion, our study identifies nuciferine as a novel ferroptosis inducer that directly targets TGF-βR1, inhibits SMAD3 signaling, and thereby downregulating GPX4 and SLC7A11 transcription, while simultaneously driving metabolic reprogramming and immunogenic cell death that sensitizes HCC to anti-PD-1 therapy **(Figure 10)**. These findings provide a robust mechanistic foundation for the clinical translation of nuciferine in HCC treatment.

Credit Author Contribution Statement

Hongwei Lan: Conceptualization, Investigation, Validation, Writing – original draft. Yang Zhou: Investigation, Methodology. Shuo Yao: Data curation, Formal analysis. Shifeng Pang: Data curation, Formal analysis, Writing – original draft; Jiayao Liu: Methodology, Conceptualization, Resources.

Animal Ethics Statement

Animal studies were approved by the Ethics Committee of Guangdong Provincial People's Hospital (S2024-816-01), where the *in vivo* experiments were conducted

Declaration of competing interest

The authors declare that they have no known competing financial interests or personal relationships that could have appeared to the work reported in this paper.

Data availability

Data will be made available on request.

Funding Declaration

This study was supported by the Natural Science Foundation of the Guangdong Province (2024A1515012937, 2022A1515010028), Guizhou Provincial People's Hospital (Grant No. [2026]-7).

References

Aldea, M., Andre, F., Marabelle, A., Dogan, S., Barlesi, F., Soria, J.C., 2021. Overcoming resistance to tumor-targeted and immune-targeted therapies. *Cancer Discov.* 11 (4), 874–899. https://doi.org/10.1158/2159-8290.CD-20-1638

Brand, A., Singer, K., Koehl, G.E., Kolitzus, M., Schoenhammer, G., Thiel, A., et al., 2016. LDHA-associated lactic acid production blunts tumor immunosurveillance by T and NK cells. *Cell Metab.* 24 (5), 657–671. https://doi.org/10.1016/j.cmet.2016.08.011

Bray, F., Laversanne, M., Sung, H., Ferlay, J., Siegel, R.L., Torre, L.A., et al., 2024. Global cancer statistics 2022: GLOBOCAN estimates of incidence and mortality worldwide for 36 cancers in 185 countries. *CA Cancer J. Clin.* 74 (3), 229–263. https://doi.org/10.3322/caac.21834

Bruni, D., Angell, H.K., Galon, J., 2020. The immune contexture and Immunoscore in cancer prognosis and therapeutic efficacy. *Nat. Rev. Cancer* 20 (11), 662–680. https://doi.org/10.1038/s41568-020-0285-7

Chen, L., Xing, X., Zhu, Y., Li, X., Wang, Y., Zhang, Y., et al., 2024. Palmitoylation alters LDHA activity and pancreatic cancer response to chemotherapy. *Cancer Lett.* 587, 216696. https://doi.org/10.1016/j.canlet.2024.216696

Cheng, A.L., Qin, S., Ikeda, M., Kim, T.Y., Kudo, M., Breder, V., et al., 2022. Updated efficacy and safety data from IMbrave150: Atezolizumab plus bevacizumab vs. sorafenib for unresectable hepatocellular carcinoma. *J. Hepatol.* 76 (4), 862–873. https://doi.org/10.1016/j.jhep.2021.11.030

Chryplewicz, A., Scotton, J., Tichet, M., Avril, T., Bausinger, H., Momier, D., et al., 2022. Cancer cell autophagy, reprogrammed macrophages, and remodeled vasculature in glioblastoma triggers tumor immunity. *Cancer Cell* 40 (10), 1111–1127.e9. https://doi.org/10.1016/j.ccell.2022.08.014

Dai, E., Chen, X., Linkermann, A., Kang, R., Tang, D., 2024. A guideline on the molecular ecosystem regulating ferroptosis. *Nat. Cell Biol.* 26 (9), 1447–1457. https://doi.org/10.1038/s41556-024-01360-8

Galon, J., Angell, H.K., Bedognetti, D., Marincola, F.M., 2013. The continuum of cancer immunosurveillance: prognostic, predictive, and mechanistic signatures. *Immunity* 39 (1), 11–26. https://doi.org/10.1016/j.immuni.2013.07.008

Galluzzi, L., Buqué, A., Kepp, O., Zitvogel, L., Kroemer, G., 2017. Immunogenic cell death in cancer and infectious disease. *Nat. Rev. Immunol.* 17 (2), 97–111. https://doi.org/10.1038/nri.2016.107

Ganesan, P., Kulik, L.M., 2023. Hepatocellular carcinoma: new developments. *Clin. Liver Dis.* 27 (1), 85–102. https://doi.org/10.1016/j.cld.2022.08.004

Guo, F., Yang, X., Li, X., Zhang, L., 2013. Nuciferine prevents hepatic steatosis and injury induced by a high-fat diet in hamsters. *PLoS One* 8 (5), e63770. https://doi.org/10.1371/journal.pone.0063770

Hanahan, D., 2022. Hallmarks of cancer: new dimensions. *Cancer Discov.* 12 (1), 31–46. https://doi.org/10.1158/2159-8290.CD-21-1059

Huang, W., Aabed, N., Shah, Y.M., 2023. Reactive oxygen species and ferroptosis at the nexus of inflammation and colon cancer. *Antioxid. Redox Signal.* 39 (7–9), 551–568. https://doi.org/10.1089/ars.2023.0246

Llovet, J.M., Castet, F., Heikenwalder, M., Mazzaferro, V., Pinyol, R., Galle, P.R., et al., 2022. Immunotherapies for hepatocellular carcinoma. *Nat. Rev. Clin. Oncol.* 19 (3), 151–172. https://doi.org/10.1038/s41571-021-00573-2

Massagué, J., 2012. TGFβ signalling in context. *Nat. Rev. Mol. Cell Biol.* 13 (10), 616–630. https://doi.org/10.1038/nrm3434

Overchuk, M., Choi, A.M., Rickard, B.P., Gomes, A.L., Hasan, M.R., Obaid, G., et al., 2025. Photodynamic therapy simultaneously induces ferroptosis- and apoptosis-like lipid signatures in ovarian cancer cells. *Cell Death Dis.* 16 (1), 899. https://doi.org/10.1038/s41419-025-08189-5

Peng, D., Fu, M., Wang, M., Wei, Y., Wei, X., 2022. Targeting TGF-β signal transduction for fibrosis and cancer therapy. *Mol. Cancer* 21 (1), 104. https://doi.org/10.1186/s12943-022-01569-x

Qiu, X., Zhou, T., Li, S., Zhang, Q., Wu, J., Wang, Y., et al., 2024. Spatial single-cell protein landscape reveals vimentin^{high} macrophages as immune-suppressive in the microenvironment of hepatocellular carcinoma. *Nat. Cancer* 5 (10), 1557–1578. https://doi.org/10.1038/s43018-024-00824-y

Sun, Y., Wu, L., Zhong, Y., Zhang, Q., Zhang, Z., Li, Y., et al., 2021. Single-cell landscape of the ecosystem in early-relapse hepatocellular carcinoma. *Cell* 184 (2), 404–421.e16. https://doi.org/10.1016/j.cell.2020.11.041

Tang, D., Chen, X., Kang, R., Kroemer, G., 2021. Ferroptosis: molecular mechanisms and health implications. *Cell Res.* 31 (2), 107–125. https://doi.org/10.1038/s41422-020-00441-1

Viswanathan, V.S., Ryan, M.J., Dhruv, H.D., Gill, S., Eichhoff, O.M., Seashore-Ludlow, B., et al., 2017. Dependency of a therapy-resistant state of cancer cells on a lipid peroxidase pathway. *Nature* 547 (7664), 453–457. https://doi.org/10.1038/nature23007

Wang, B., Wu, L., Chen, J., Zhang, Y., 2021. Metabolism pathways of arachidonic acids: mechanisms and potential therapeutic targets. *Signal Transduct. Target. Ther.* 6 (1), 94. https://doi.org/10.1038/s41392-020-00443-w

Wang, H., Liu, D., Zheng, B., Li, J., Zhang, Y., 2023. Emerging role of ferroptosis in diabetic kidney disease: molecular mechanisms and therapeutic opportunities. *Int. J. Biol. Sci.* 19 (9), 2678–2694. https://doi.org/10.7150/ijbs.81892

Xie, J.R., Chen, X.J., Zhou, G., 2023. Nuciferine inhibits oral squamous cell carcinoma partially through suppressing the STAT3 signaling pathway. *Int. J. Mol. Sci.* 24 (19), 14532. https://doi.org/10.3390/ijms241914532

Xiong, Z., Chan, S.L., Zhou, J., Li, Y., Chen, L., Huang, D., et al., 2023. Targeting PPAR-gamma counteracts tumour adaptation to immune-checkpoint blockade in hepatocellular carcinoma. *Gut* 72 (9), 1758–1773. https://doi.org/10.1136/gutjnl-2022-328364

Zhao, T., Zhu, Y., Zhao, R., Li, X., Wang, Y., 2023. Structure-activity relationship, bioactivities, molecular mechanisms, and clinical application of nuciferine on inflammation-related diseases. *Pharmacol. Res.* 193, 106820. https://doi.org/10.1016/j.phrs.2023.106820

Zhou, Q., Meng, Y., Li, D., Wang, H., Zhang, Y., 2024. Ferroptosis in cancer: from molecular mechanisms to therapeutic strategies. *Signal Transduct. Target. Ther.* 9 (1), 55. https://doi.org/10.1038/s41392-024-01769-5

Zhou, L., Lian, G., Zhou, T., Zhang, Y., Wang, X., Li, Z., et al., 2025. Palmitoylation of GPX4 via the targetable ZDHHC8 determines ferroptosis sensitivity and antitumor immunity. *Nat. Cancer* 6 (5), 768–785. https://doi.org/10.1038/s43018-025-00937-y

Zitvogel, L., Kepp, O., Kroemer, G., 2011. Immune parameters affecting the efficacy of chemotherapeutic regimens. *Nat. Rev. Clin. Oncol.* 8 (3), 151–160. https://doi.org/10.1038/nrclinonc.2010.223

Figure Legends

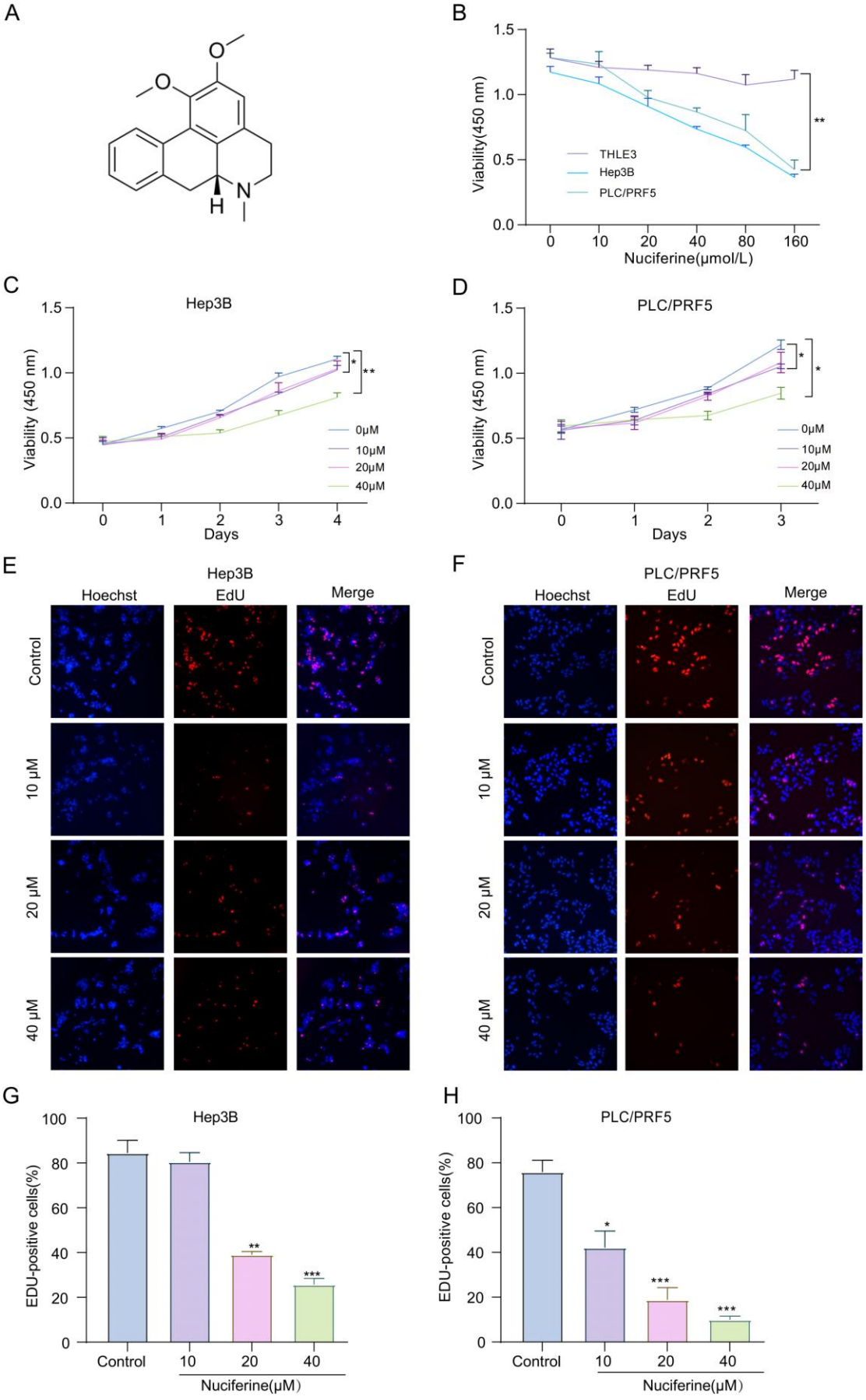

Figure 1. Nuciferine inhibits the viability and proliferation of hepatocellular carcinoma

cells. (A) Chemical structure of nuciferine. (B) Cell viability of normal liver THLE3 cells and hepatocellular carcinoma Hep3B and PLC/PRF/5 cells treated with different concentrations of nuciferine, as determined by CCK-8 assay. (C, D) Time-dependent changes in cell viability of Hep3B and PLC/PRF/5 cells after treatment with different concentrations of nuciferine. (E, F) EdU staining showing the effect of nuciferine on the proliferation of Hep3B and PLC/PRF/5 cells. Hoechst was used to stain nuclei, and EdU-positive cells are shown in red. (G, H) Quantification of EdU-positive cells, indicating that nuciferine significantly reduced the proliferation of Hep3B and PLC/PRF/5 cells.

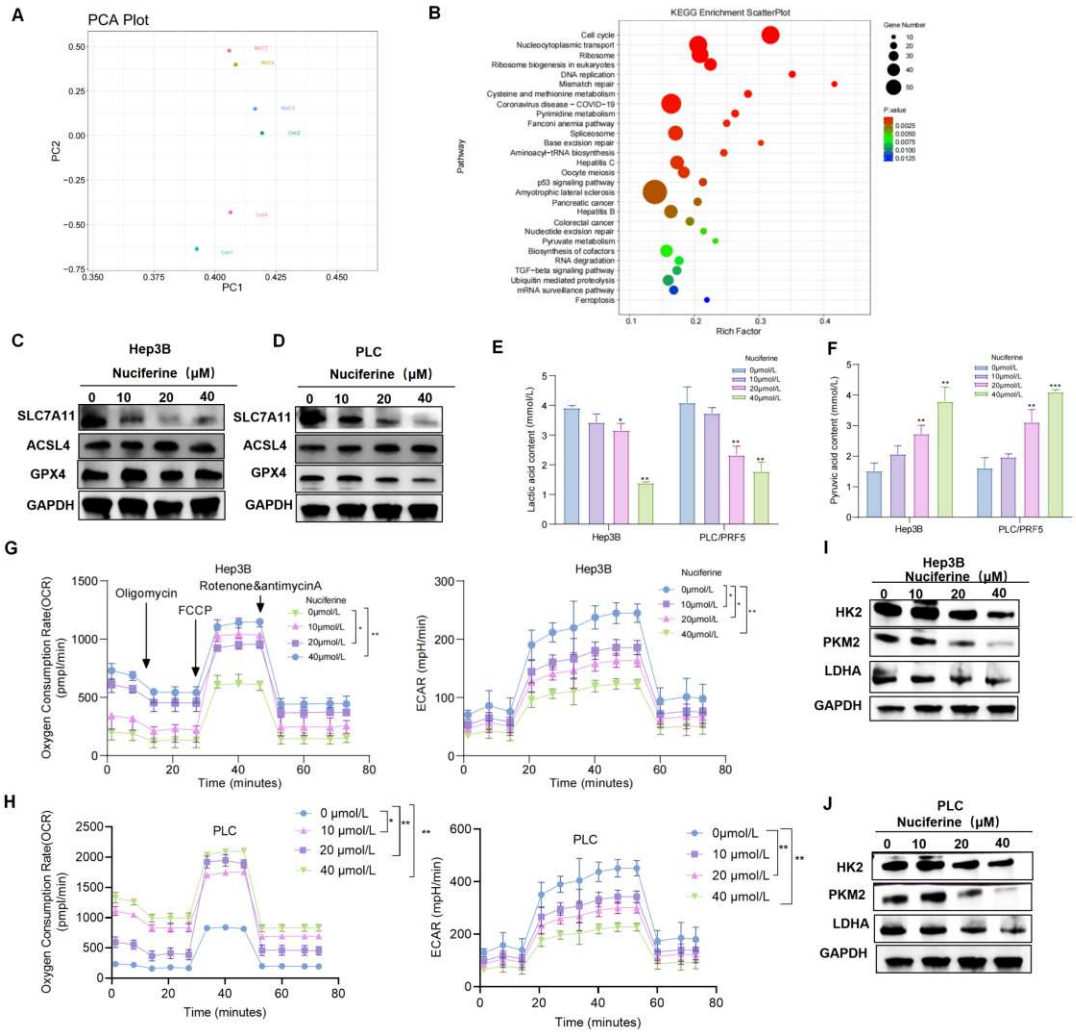

Figure 2. Nuciferine induces metabolic reprogramming in HCC cells. (A) PCA score plot of transcriptomic profiles from control and nuciferine-treated HCC cells. (B) KEGG enrichment scatter plot of differentially expressed genes in nuciferine-treated HCC cells. (C, D) Western blotting of SLC7A11, ACSL4, and GPX4 in Hep3B (C) and PLC/PRF/5 (D) cells treated with nuciferine (0 – 40 μ mol/L). (E, F) Intracellular lactic acid (E) and pyruvic acid (F) contents in Hep3B and PLC/PRF/5 cells. (G, H) Oxygen consumption rate (OCR) and extracellular acidification rate (ECAR) measured by Seahorse XF96 analysis in Hep3B (G) and PLC/PRF/5 (H) cells treated with nuciferine. (I, J) Western blotting of the glycolytic

enzymes HK2, PKM2, and LDHA in Hep3B (I) and PLC/PRF/5 (J) cells. Data are presented as mean ± SD. *P < 0.05, **P < 0.01, ***P < 0.001.

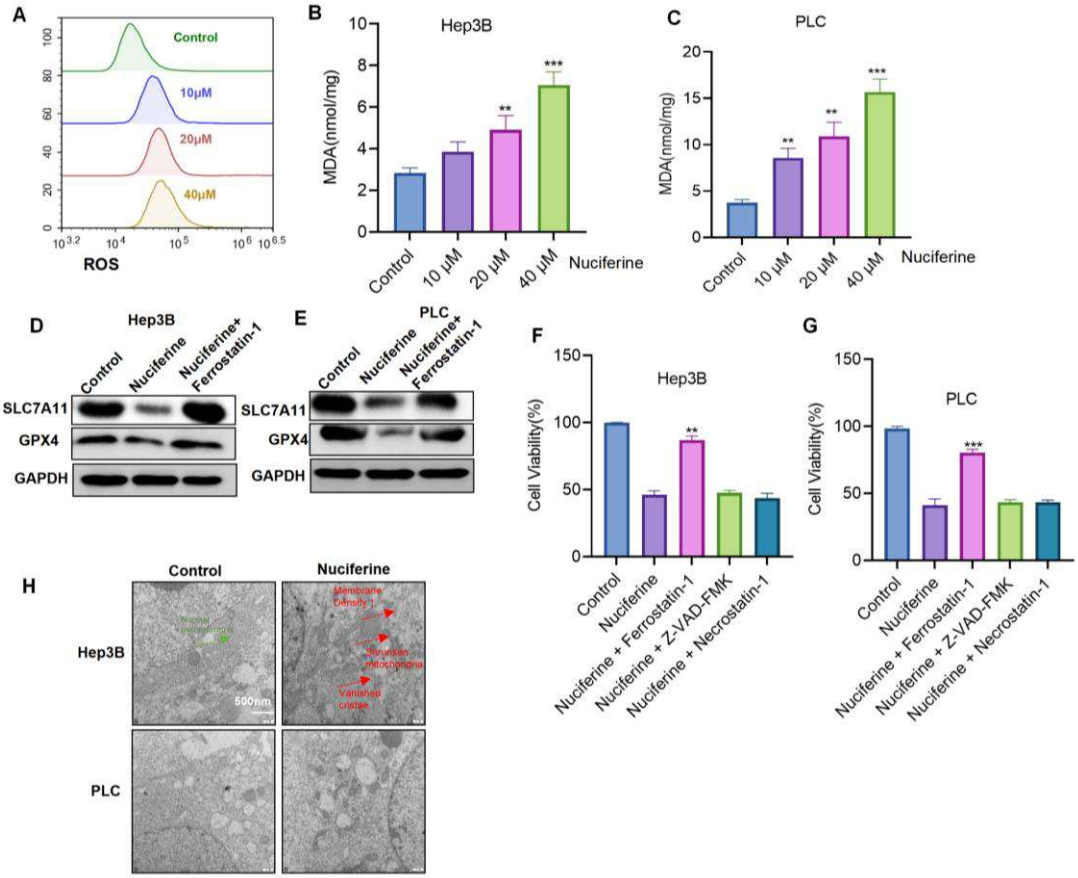

Figure 3. Nuciferine triggers ferroptosis in HCC cells. (A) Intracellular ROS levels detected by flow cytometry (DCFH-DA) in Hep3B cells treated with increasing concentrations of nuciferine (0 – 40 μ mol/L). (B, C) MDA levels in Hep3B (B) and PLC/PRF/5 (C) cells treated with nuciferine. (D, E) Western blotting of SLC7A11 and GPX4 in Hep3B (D) and PLC/PRF/5 (E) cells treated with nuciferine with or without ferrostatin-1. (F, G) Cell viability of Hep3B (F) and PLC/PRF/5 (G) cells treated with nuciferine in the presence of ferrostatin-1, Z-VAD-FMK, or necrostatin-1. (H) Transmission electron microscopy of mitochondrial morphology in control and nuciferine-treated Hep3B and PLC/PRF/5 cells; red arrows indicate shrunken mitochondria with increased membrane density. Data are presented as mean ± SD. *P < 0.05, **P < 0.01, ***P < 0.001.

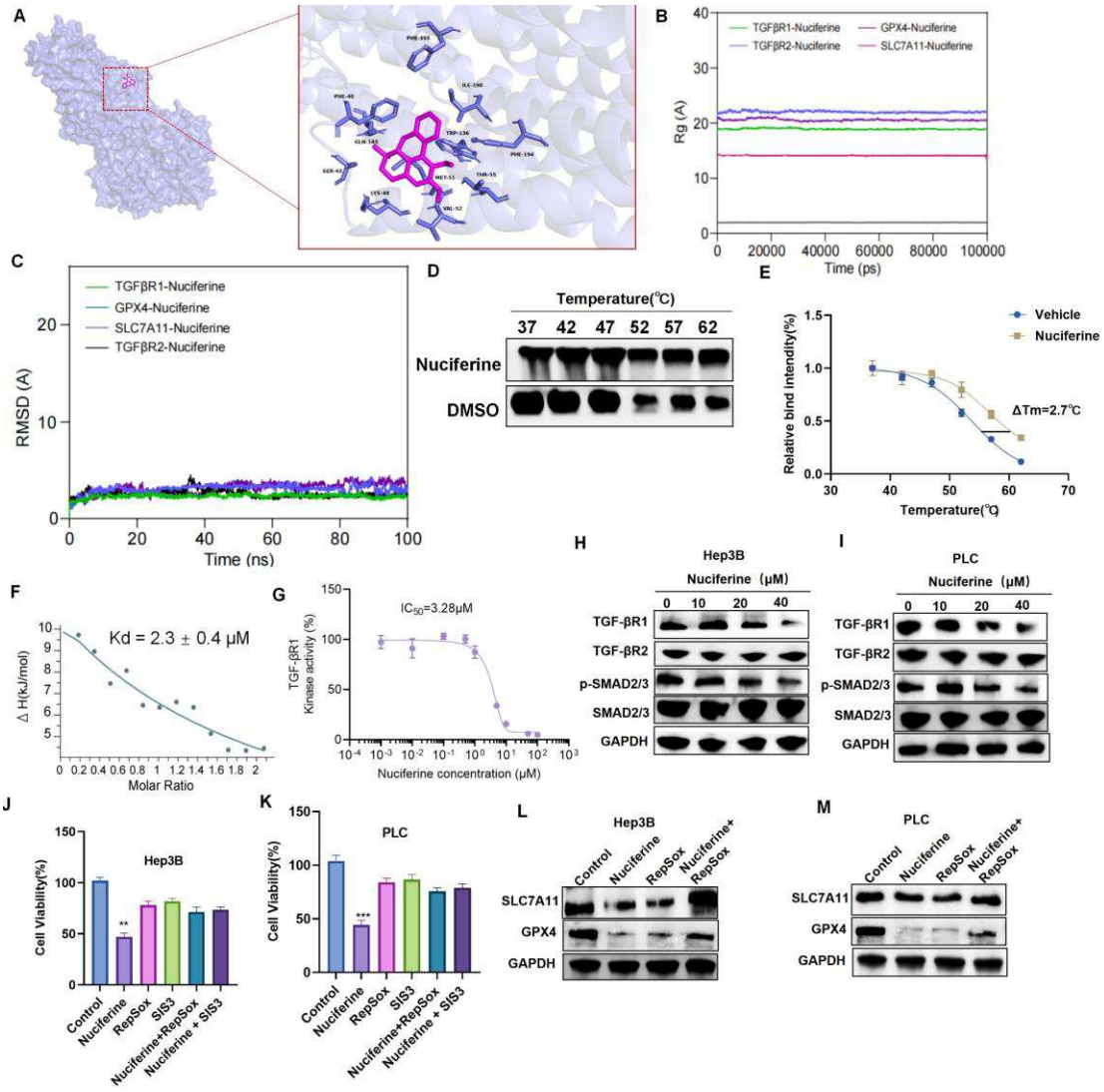

Figure 4. Nuciferine directly binds to TGF-βR1 and inhibits its kinase activity and downstream SMAD3 signaling. (A) Molecular docking model showing nuciferine (magenta) binding to the ATP-binding pocket of TGF-βR1; key interacting residues are indicated. (B, C) Radius of gyration (Rg; B) and root-mean-square deviation (RMSD; C) from 100-ns MD simulations of nuciferine in complex with TGF-βR1, TGF-βR2, GPX4, or SLC7A11. (D, E) Cellular thermal shift assay (CETSA) showing the thermal stabilization of TGF-βR1 by nuciferine (ΔTm = 2.7 °C). (F) Isothermal titration calorimetry (ITC) analysis of the nuciferine–TGF-βR1 interaction (Kd = 2.3 ± 0.4 μmol/L). (G) TGF-βR1 kinase activity assay showing dose-dependent inhibition by nuciferine (IC50 = 3.28 μmol/L). (H, I) Western blotting of TGF-βR1, TGF-βR2, p-SMAD2/3, and total SMAD2/3 in Hep3B (H) and PLC/PRF/5 (I) cells treated with nuciferine (0–40 μmol/L). (J, K) Cell viability of Hep3B (J) and PLC/PRF/5 (K) cells treated with nuciferine, RepSox, and/or SIS3 as indicated. (L, M) Western blotting of SLC7A11 and GPX4 in Hep3B (L) and PLC/PRF/5 (M) cells treated with nuciferine with or without RepSox. Data are presented as mean ± SD. *P < 0.05, **P < 0.01, ***P < 0.001.

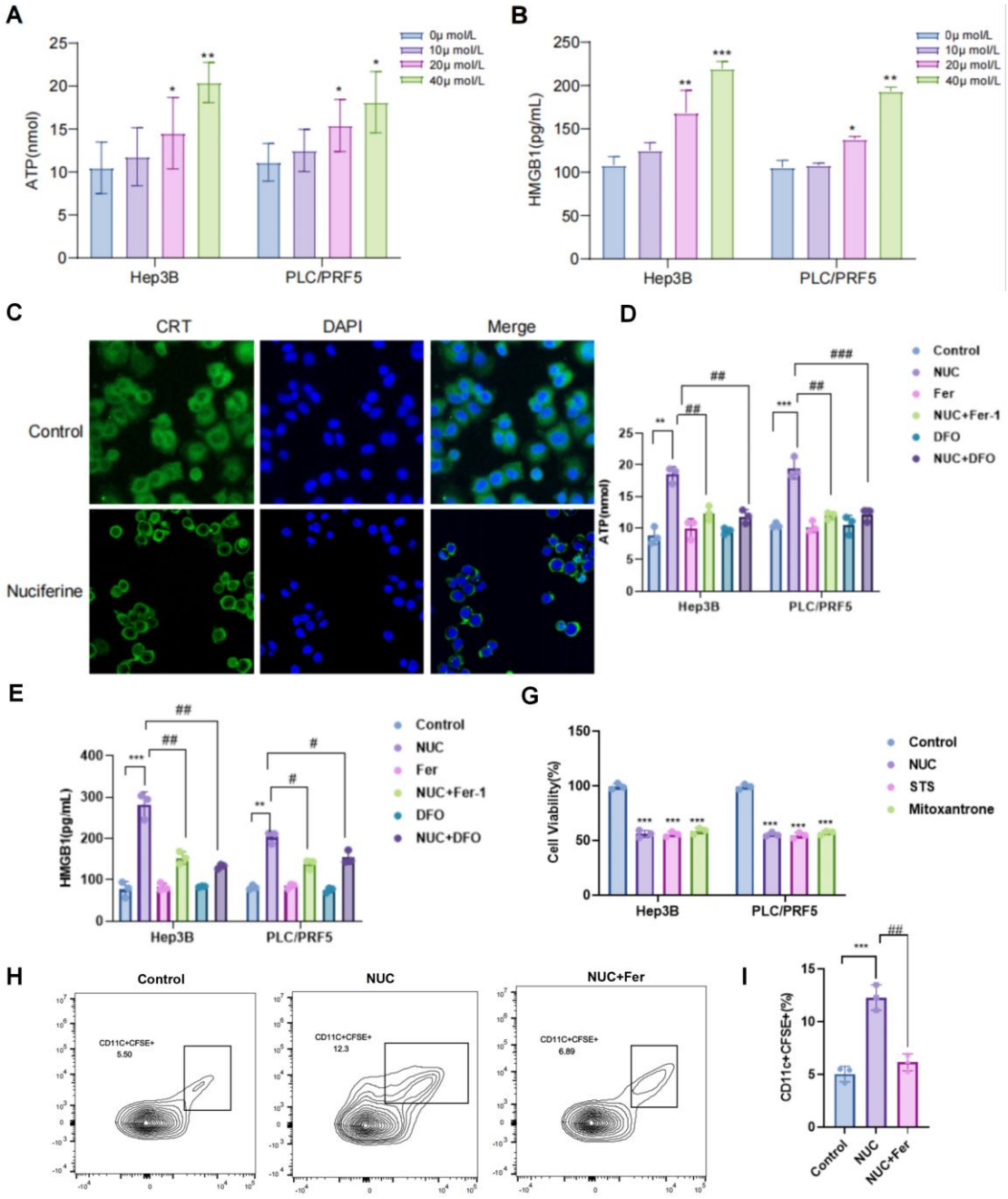

Figure 5. Nuciferine-induced ferroptosis triggers immunogenic cell death in HCC cells. (A, B) Extracellular ATP (A) and HMGB1 (B) release from Hep3B and PLC/PRF/5 cells treated with increasing concentrations of nuciferine (0 – 40 μ mol/L). (C) Immunofluorescence staining of calreticulin (CRT) membrane exposure in control and nuciferine-treated cells. (D, E) ATP (D) and HMGB1 (E) release from Hep3B and PLC/PRF/5 cells treated with nuciferine in the presence of the indicated ferroptosis modulators (Fer, ferrostatin-1, or DFO). (G) Cell viability of Hep3B and PLC/PRF/5 cells treated with nuciferine, staurosporine (STS), or mitoxantrone. (H, I) Representative flow cytometric analysis (H) and quantification (I) of dendritic cell phagocytosis (CD11c+CFSE+) of CFSE-labeled Hep3B cells treated with nuciferine with or without ferrostatin-1. Data are presented as mean ± SD. *P < 0.05, **P < 0.01, ***P < 0.001; #P < 0.05, ##P < 0.01, ###P < 0.001.

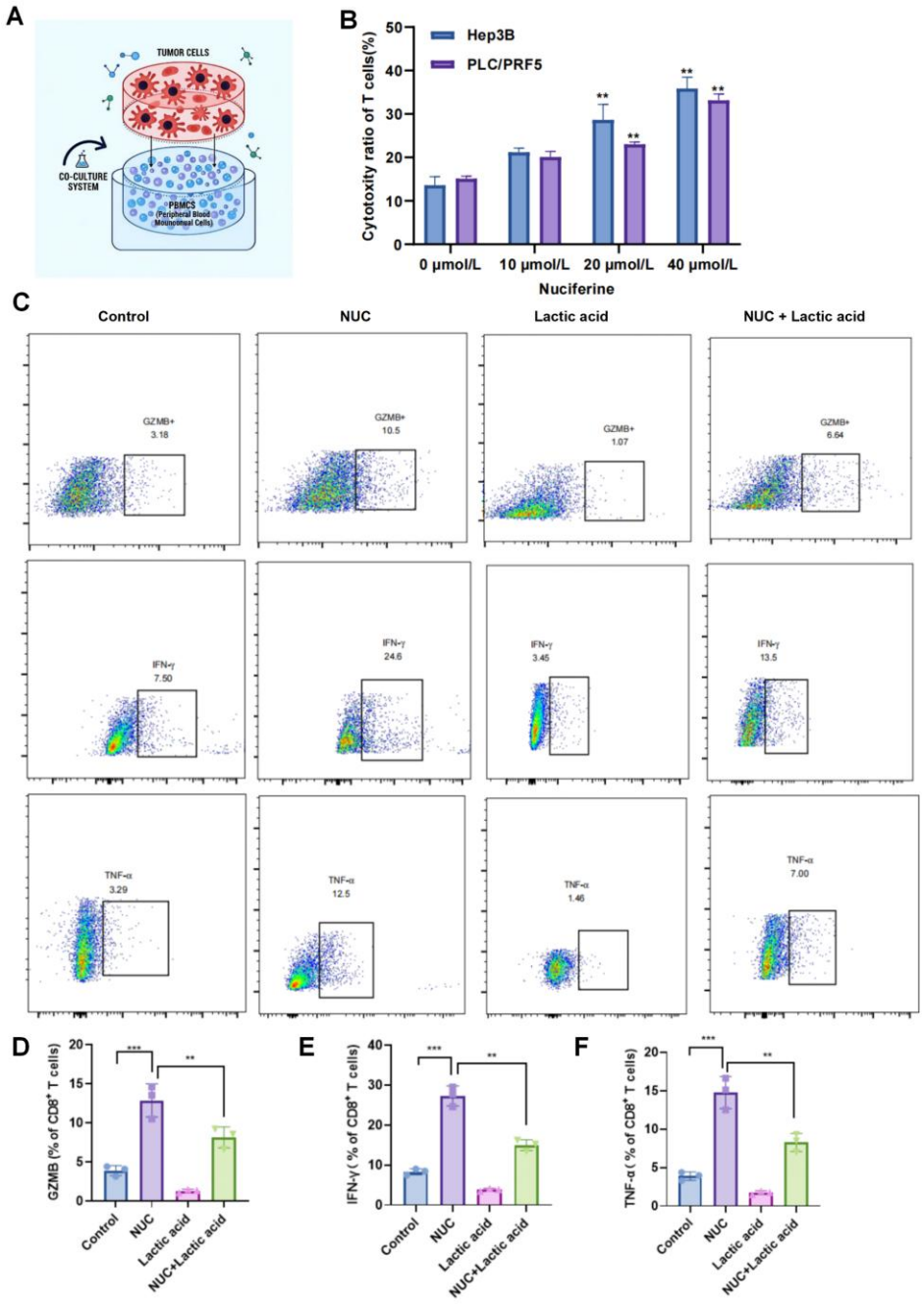

Figure 6. Nuciferine enhances T-cell-mediated killing of HCC cells, an effect attenuated by lactic acid. (A) Schematic illustration of the tumor cell–PBMC co-culture system. (B) Cytotoxicity ratio of T cells against Hep3B and PLC/PRF/5 cells treated with increasing concentrations of nuciferine (0–40 μmol/L). (C) Representative flow cytometric analysis of GZMB, IFN-γ, and TNF-α expression in CD8+ T cells co-cultured under control, nuciferine, lactic acid, and nuciferine plus lactic acid conditions. (D–F) Quantification of GZMB+ (D), IFN-γ + (E), and TNF-α + (F) cells among CD8+ T cells. Data are presented as mean ± SD. *P < 0.05, **P < 0.01, ***P < 0.001.

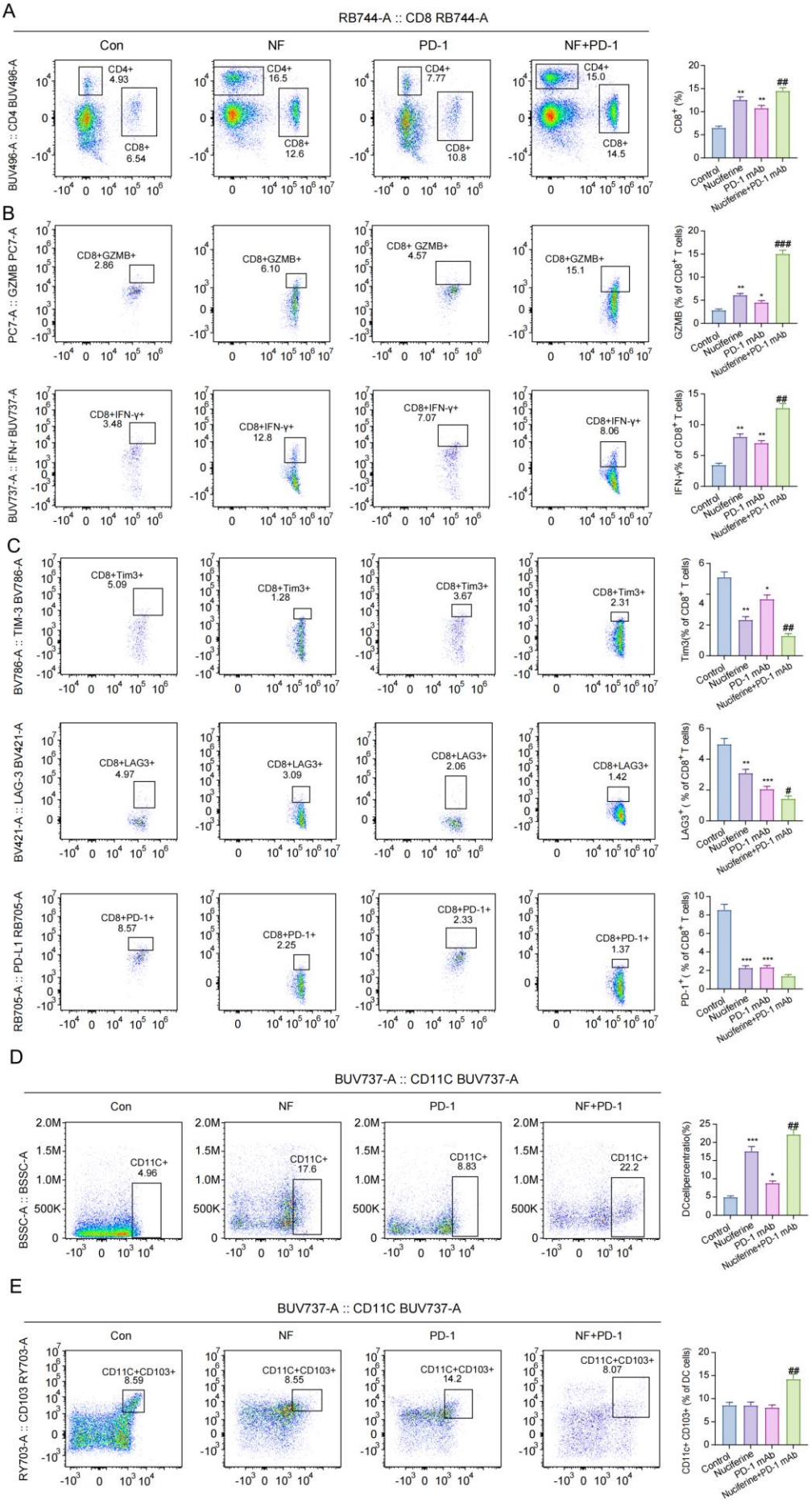
A
RB744-A :: CD8 RB744-A
Con
NF
PD-1
NF+PD-1
BUV496-A :: CD4 BUV496-A
CD4+ 4.93
CD8+ 6.54
CD4+ 16.5
CD8+ 12.6
CD4+ 7.77
CD8+ 10.8
CD4+ 15.0
CD8+ 14.5
CD8+ (%)
B
PC7-A :: GZMB PC7-A
CD8+GZMB+ 2.86
CD8+GZMB+ 6.10
CD8+ GZMB+ 4.57
CD8+GZMB+ 15.1
GZMB (% of CD8+ T cells)
BUV737-A :: IFN-γ BUV737-A
CD8+IFN-γ+ 3.48
CD8+IFN-γ+ 12.8
CD8+IFN-γ+ 7.07
CD8+IFN-γ+ 8.06
IFN-γ% of CD8+ T cells)
C
BV786-A :: TIM-3 BV786-A
CD8+Tim3+ 5.09
CD8+Tim3+ 1.28
CD8+Tim3+ 3.67
CD8+Tim3+ 2.31
Tim3(% of CD8+ T cells)
BV421-A :: LAG-3 BV421-A
CD8+LAG3+ 4.97
CD8+LAG3+ 3.09
CD8+LAG3+ 2.06
CD8+LAG3+ 1.42
LAG3+ (% of CD8+ T cells)
RB705-A :: PD-L1 RB705-A
CD8+PD-1+ 8.57
CD8+PD-1+ 2.25
CD8+PD-1+ 2.33
CD8+PD-1+ 1.37
PD-1+ (% of CD8+ T cells)
Control
Nuciferine
PD-1 mAb
Nuciferine+PD-1 mAb
D
BUV737-A :: CD11C BUV737-A
Con
NF
PD-1
NF+PD-1
BSSC-A :: BSSC-A
CD11C+ 4.96
CD11C+ 17.6
CD11C+ 8.83
CD11C+ 22.2
DCcellpercentratio(%)
E
BUV737-A :: CD11C BUV737-A
Con
NF
PD-1
NF+PD-1
RY703-A :: CD103 RY703-A
CD11C+CD103+ 8.59
CD11C+CD103+ 8.55
CD11C+CD103+ 14.2
CD11C+CD103+ 8.07
CD11c+ CD103+ (% of DC cells)

631

Figure 7. Nuciferine synergizes with anti-PD-1 therapy to suppress HCC growth in immunocompetent mice. (A) Schematic illustration of the subcutaneous Hepa1-6 tumor model in C57BL/6J mice; nuciferine (100 mg/kg) was administered every 3 days, with or without anti-PD-1 mAb, and mice were sacrificed on day 21. (B) Photographs of excised tumors from the four groups. (C, D) Tumor growth curves (C) and tumor weights at endpoint (D). (E) Immunofluorescence staining of CD8, TNF-α, and IFN-γ in tumor sections. (F) Immunohistochemical staining of Ki67 and GPX4 in tumor tissues. (G) Western blotting of ACSL4, GPX4, HK2, Ki67, CRT, and HMGB1 in tumor tissues. Data are presented as mean ± SD. *P < 0.05, **P < 0.01; #P < 0.05, ##P < 0.01.

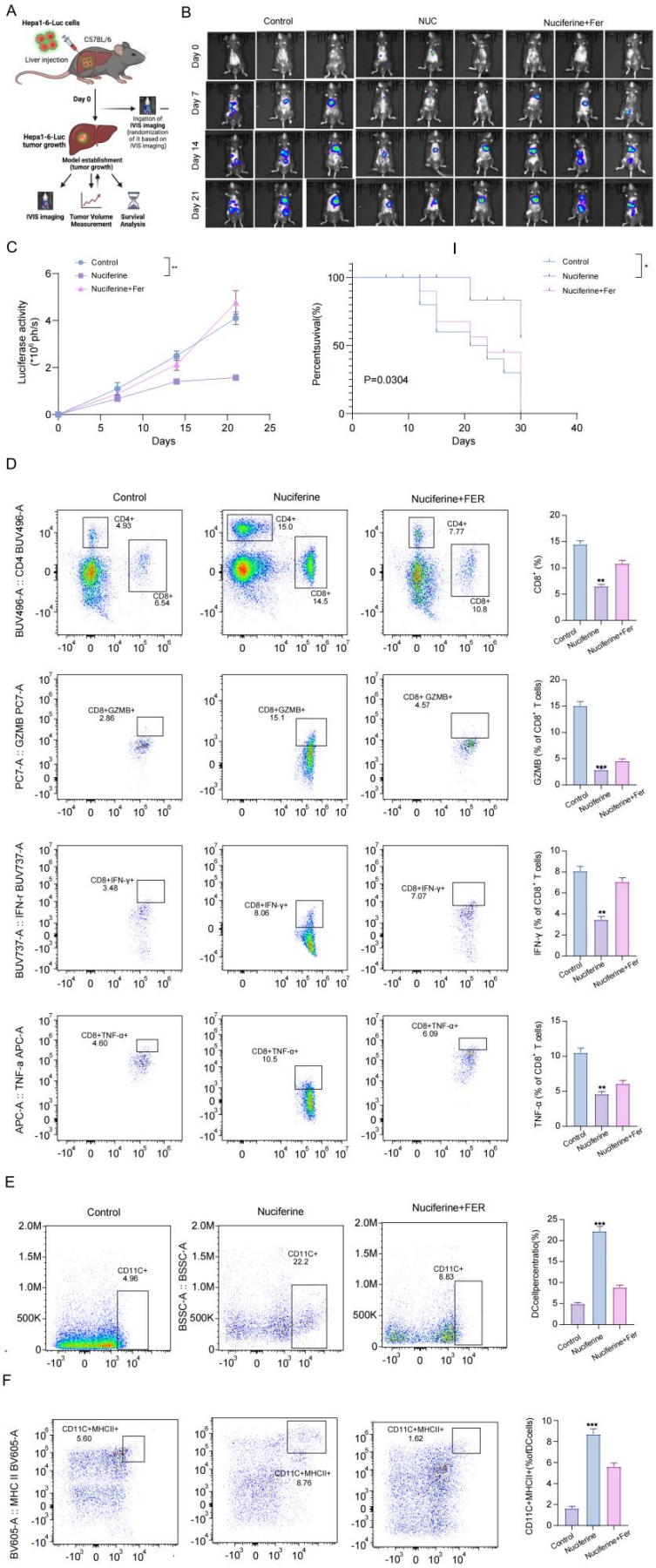
A
Hepa1-6-Luc cells
C57BL/6
Liver injection
Day 0
Ingation of IVIS imaging (randomization of it based on IVIS imaging)
Hepa1-6-Luc tumor growth
Model establishment (tumor growth)
IVIS imaging
Tumor Volume Measurement
Survival Analysis
B
Control
NUC
Nuciferine+Fer
Day 0
Day 7
Day 14
Day 21
C
Control
Nuciferine
Nuciferine+Fer
Luciferase activity (*10⁶ ph/s)
Days
I
Percentsuvival(%)
P=0.0304
D
Control
Nuciferine
Nuciferine+FER
BUV496-A :: CD4 BUV496-A
CD4+ 4.93
CD8+ 6.54
CD4+ 15.0
CD8+ 14.5
CD4+ 7.77
CD8+ 10.8
CD8+ (%)
PC7-A :: GZMB PC7-A
CD8+GZMB+ 2.86
CD8+GZMB+ 15.1
CD8+ GZMB+ 4.57
GZMB (% of CD8+ T cells)
BUV737-A :: IFN-r BUV737-A
CD8+IFN-γ+ 3.48
CD8+IFN-γ+ 8.06
CD8+IFN-γ+ 7.07
IFN-γ (% of CD8+ T cells)
APC-A :: TNF-a APC-A
CD8+TNF-α+ 4.60
CD8+TNF-α+ 10.5
CD8+TNF-α+ 6.09
TNF-α (% of CD8+ T cells)
E
Control
Nuciferine
Nuciferine+FER
BSSC-A :: BSSC-A
CD11C+ 4.96
CD11C+ 22.2
CD11C+ 8.83
DCcellpercentratio(%)
F
BV605-A :: MHC II BV605-A
CD11C+MHCII+ 5.60
CD11C+MHCII+ 8.76
CD11C+MHCII+ 1.62
CD11C+MHCII+(%ofDCcells)

642

Figure 8. Nuciferine combined with anti-PD-1 therapy remodels the tumor immune microenvironment. Tumor-infiltrating immune cells from the four groups (Control, Nuciferine, PD-1 mAb, Nuciferine + PD-1 mAb) were analyzed by flow cytometry. (A) Representative plots and quantification of CD4+ and CD8+ T cells. (B) GZMB+ and IFN- γ + cells among CD8+ T cells. (C) Expression of the exhaustion markers Tim-3, LAG-3, and PD-1 on CD8+ T cells. (D) Proportion of CD11c+ dendritic cells. (E) Proportion of CD11c+CD103+ dendritic cells. (F) Expression of CD40 and MHC II on CD11c+ dendritic cells. Data are presented as mean ± SD. *P < 0.05, **P < 0.01, ***P < 0.001; #P < 0.05, ##P < 0.01, ###P < 0.001.

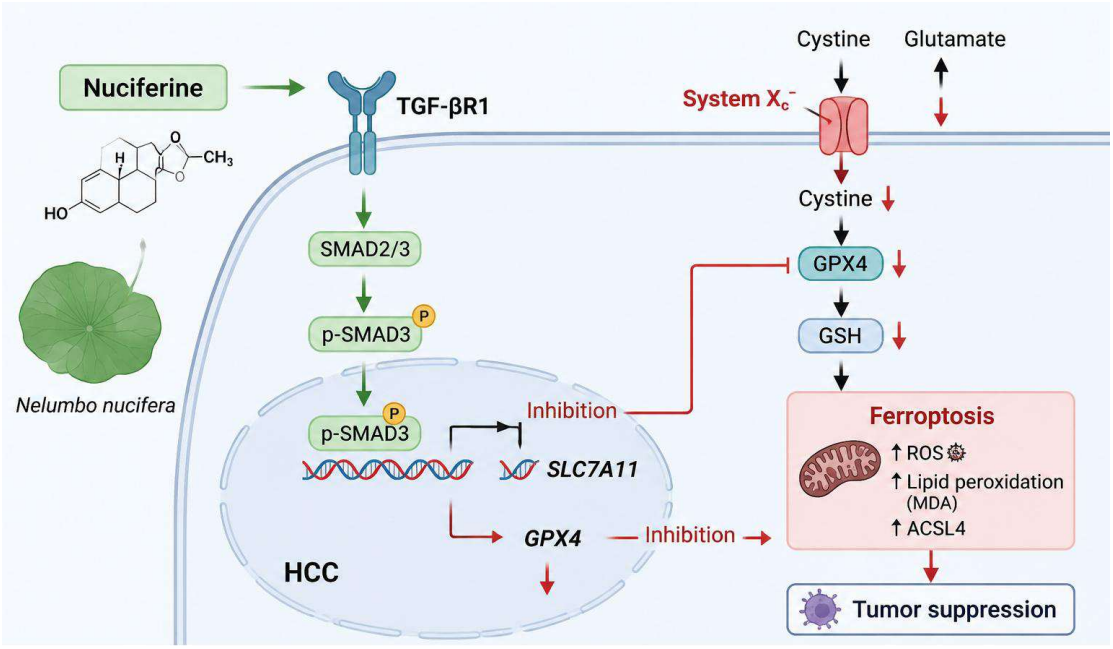

Figure 9. Nuciferine suppresses orthotopic HCC growth and activates anti-tumor immunity in a ferroptosis-dependent manner. (A) Schematic illustration of the orthotopic Hepa1-6-Luc liver tumor model in C57BL/6J mice. (B) Representative IVIS bioluminescence images on days 0, 7, 14, and 21. (C) Quantification of luciferase activity over time. (I) Kaplan–Meier survival curves (P = 0.0304). (D) Flow cytometric analysis and quantification of CD8+, CD8+GZMB+, CD8+IFN-γ+, and CD8+TNF-α+ T cells in tumors. (E, F) Flow cytometric analysis and quantification of CD11c+ (E) and CD11c+MHC II+ (F) dendritic cells. Data are presented as mean ± SD. *P < 0.05, **P < 0.01, ***P < 0.001.

Figure 10. Schematic illustration of the proposed mechanism by which nuciferine induces ferroptosis in hepatocellular carcinoma (HCC).

Nuciferine, a natural alkaloid from lotus leaves, directly binds and inhibits TGF-βR1, blocking SMAD3 activation. This downregulates SLC7A11 and GPX4, collapses antioxidant defenses, and triggers ferroptosis and immunogenic cell death, thereby suppressing hepatocellular carcinoma and synergizing with anti-PD-1 therapy.

Result

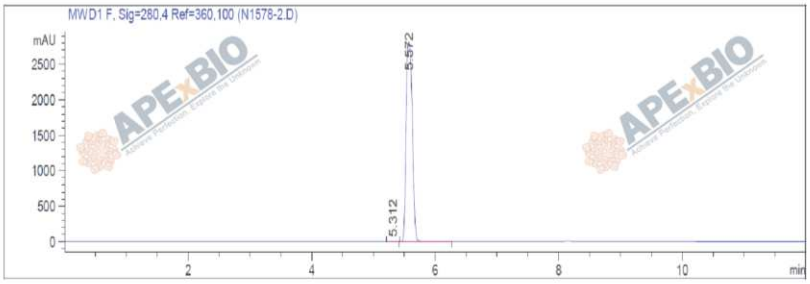

Rank	RetTime(min)	Area(mAU*s)	Area %
1	5.312	9.43982	0.0480
2	5.572	1.96643e4	99.9520

Caution

FOR RESEARCH PURPOSES ONLY.

NOT FOR HUMAN, VETERINARY DIAGNOSTIC OR THERAPEUTIC USE.

APExBIO Technology

www.apexbt.com

7505 Fannin street, Suite 410, Houston, TX 77054.

Tel: +1-832-696-8203 | Fax: +1-832-641-3177 | Email: info@apexbt.com

Figure S1. HPLC purity analysis of nuciferine.

Representative high-performance liquid chromatography (HPLC) chromatogram and peak-integration results for nuciferine. The retention time, peak area, and relative peak area are shown. The major peak was detected at 5.572 min and accounted for 99.952% of the total peak area, whereas the minor peak at 5.312 min accounted for 0.048%, indicating a purity of 99.952%.

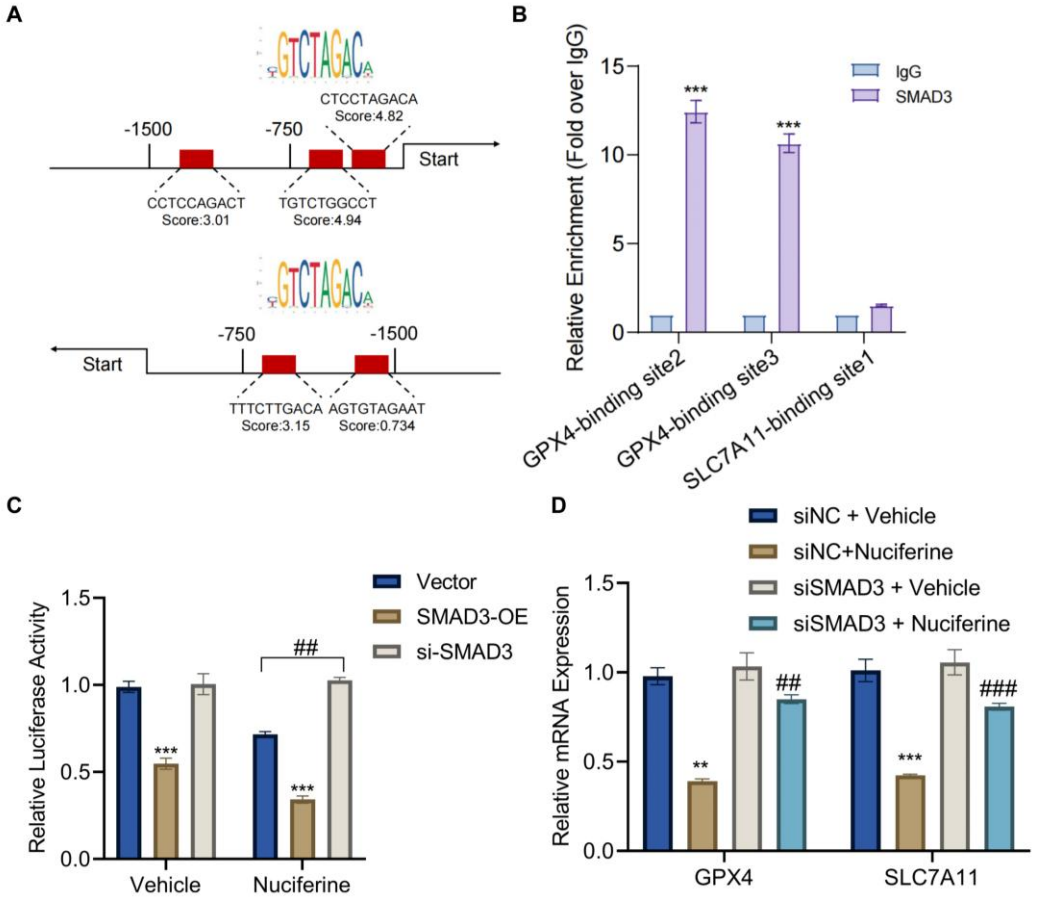

Figure S2. SMAD3 transcriptionally regulates GPX4 and SLC7A11 in hepatocellular carcinoma cells.

(A) Schematic illustration of the predicted SMAD3-binding motifs and potential SMAD3-binding sites within the promoter regions of GPX4 and SLC7A11.

(B) Chromatin immunoprecipitation followed by quantitative PCR (ChIP-qPCR) showing

SMAD3 enrichment at the indicated GPX4 and SLC7A11 promoter regions. IgG was used as the negative control.

(C) Dual-luciferase reporter assay showing the effects of SMAD3 overexpression or knockdown on promoter activity in cells treated with vehicle or nuciferine.

(D) Quantitative reverse-transcription PCR analysis of GPX4 and SLC7A11 mRNA expression in control or SMAD3-knockdown cells treated with vehicle or nuciferine.

Supplementary Files

This is a list of supplementary files associated with this preprint. Click to download.

- S2.png
- fulluncroppedGelsandBlotsimages.zip
- S102.tif